The Module for Event Driven Operations on Spacecraft (MEDOS)

Alexander C. Barrie, Miles Bengtson, Liam Greenlee, Joseph Patton, Ryan Kinney, Connor Firth and Stewart Doe
Aurora Engineering, Potomac, MD, 20854, USA

Paul Wood and Robert Klar
Southwest Research Institute, San Antonio, TX, 78238, USA

Russel Bjella, Brandon Stone, Marcus Piquette and Christopher Pankratz
University of Colorado, Laboratory for Atmospheric and Space Physics, Boulder, CO, 80303, USA

Wayne Yu
NASA/GSFC, Greenbelt, MD, 20771, USA

The Module for Event Driven Operations on Spacecraft (MEDOS) is a framework for real time operational decisions based on detected events from on-board measurements. MEDOS calculates derived parameters, which are physically meaningful and relevant to a mission planner. These derived parameters are then compared, using fuzzy sets, to typical (e.g. published) values of the given parameter and a confidence is produced that the event in question has occurred. Operational responses can then be triggered to detected events. MEDOS has been validated using raw flight data from the MMS mission, and has been verified on flight hardware for a NASA TRL-6 rating. Because MEDOS utilizes processes well understood and developed by the community in question, and due to the nature of events being presented as a likelihood rather than a definitive, it achieves a level of trust that can enable future mission infusion for operational space missions.

I. Introduction

Operations engineers face the task of maintaining successful operation of a spacecraft based on extremely limited information. This task becomes even more complicated when considering lag time between contacts, the light-time delay of bidirectional communications, and the prospect of multiple spacecraft operating simultaneously. Imagine a swarm of 100 satellites near Jupiter, and the prospect of manually detecting, assessing, and responding to every potential event on a spacecraft quickly approaches a point of impossibility. Simple pre-programmed time tagged commands become increasingly burdensome in multi-spacecraft missions, particularly when trying to target ephemeral events in space that are difficult to predict with any accuracy.

As Freed[1], Abbass[2], and others have outlined, autonomy is an admirable goal, and indeed NASA has outlined a technology roadmap toward spacecraft autonomy[3], but widespread adoption remains elusive as the system must

be trusted in order to be adopted by flight missions. Spacecraft commanding and operational planning is typically performed via preprogrammed time sequences[4]. In some ways, this in itself is autonomous operation: a sequence of commands is loaded that run automatically at a predefined time. This system is not responsive, or adaptive, however.

The roots of event driven operations, however, have long been present. Many spacecraft have had fault detection and correction (FDC) systems that respond to specific events and issue a corrective action[5]. Similar automated systems are often in place for routine tasks such as heater cycling[6]. The Aeronomy of Ice in the Mesosphere (AIM) spacecraft took this a step further when it lost reliable ground communications and had to automate almost all onboard operations, such as eclipse operations based on an event driven detection of eclipse exit[7]. Members of our team were themselves intimately involved in the effort to implement this onboard operations plan for AIM. There have been some failures along the way, such as NASA's DART spacecraft failing an automated docking procedure[8], however autonomous maneuver planning was successfully demonstrated by NASA's EO-1 spacecraft[9]. The James Webb Space Telescope (JWST) program noted that the Hubble Space Telescope (HST) would consistently lose time when a particular measurement could not initialize. Rather than waiting for the next schedule operation to start, JWST detects that failed measurement, and immediately moves on to the next one[10].

With the advancement of artificial intelligence (AI) and machine learning (ML), a myriad of algorithms have been proposed for spacecraft autonomy. A host of studies have been performed in the field of anomaly/outlier detection[11–13]. The use of AI/ML for maneuver planning has matured slightly further, with the work of Schaub and others[14–17], notably on the NASA Starling mission[18]. Recently, the OPS-SAT satellite has utilized a trained AI/ML algorithm to detect target areas of interest for science acquisition[19] and da Silva[20] and [21] have used ML for region classification and boundary detection.

Historically, autonomous spacecraft operations have therefore been split into two major camps: rule based, and statistical based optimizations. Strict, rule based systems are fairly straightforward to implement and can be used effectively to respond to specific events for which they have been programmed. For example, if a temperature drops too low then turn on a heater:

IF (A AND B AND C) THEN D.

But what if parameters skirt the edge of a decision point?

(A AND B AND *almost but not quite* C)

Rule based systems cannot be expected to understand every possible permutation of telemetry that they encounter, particularly when most spacecraft have thousands of telemetry points.

Statistical systems, often based on machine learning (ML), use examples of known scenarios to train a system to recognize them. If the system sees 1000 examples of an event, it can learn to recognize the signatures of that event[22].

Flight missions, however, often cannot sacrifice mission time to collecting training data. Even when data are available, the trained system is seen as a black box that is not grounded in a physical understanding of the system and an operations engineer is not able to tune or modify the model as the mission evolves.

MEDOS realizes a third approach – we put the operations engineer on the spacecraft. MEDOS takes raw telemetry and fuses them together into extracted features, creating physically meaningful derived quantities that an engineer understands. For example, turning voltages and decay times into "methane concentration", or turning count rates and field vectors into "plasma density". Then, using fuzzy sets, MEDOS compares the physical parameters to generalized event definitions that scientists and engineers use all the time in their analysis gathered from published studies, flight heritage, and subject matter expertise – "when the plasma density jumps and the magnetic field reverses direction, it means we crossed the magnetopause."

MEDOS can then be used to detect all manner of events and respond to them in real time. For example:

- Boundary crossings can be used to trigger a change in operational mode.
- Subtle signatures in science data, that can potentially be missed by human review, can be detected and flagged for downlink.
- A dangerous event, such as a coronal mass ejection (CME) can be trigger a safing event in a fleet of satellites.

MEDOS is able to analyze the ambient environment in real time, make an assessment as to what is occurring, and respond to it in a way consistent with the response of an operations engineer. MEDOS can be deployed in large constellations, far from human assistance, and can incorporate data from other spacecraft into the decision making process (for example, a lead spacecraft's measurement may be used to compute a gradient, or used as an early indication of an upcoming event.) It can be used to rank high priority data, trigger opportunistic measurements, change operating modes, monitor health and safety, perform region classification, or many other operations that can be triggered by in-situ event detection. In short, MEDOS is a step forward towards the goal of true trusted autonomy.

MEDOS can be run through NASA's core Flight System (cFS)[23], the Robot Operating System (ROS)[24], or as a custom C library which can be wrapped into other frameworks.*Note: a MEDOS implementation in JPL's F' [25] is also planned.* MEDOS has been validated to NASA Technical Readiness Level 6 (TRL-6) via flatsat testing. Space flight demonstrations are in preparation for the near future.

The remainder of this paper uses data from NASA's Magnetospheric Multiscale (MMS) mission[26] to illustrate the utility of MEDOS and is organized as follows: Section 2 describes the MEDOS algorithm, Section 3 showcases the verification and validation approach, and Section 4 provides a conclusion and future direction.

II. Core MEDOS Algorithms

The MEDOS algorithm and software consists of two stages:

1) A derived telemetry feature extractor that fuses multiple telemetry streams together into a physically meaningful

quantity

2) Event detection using fuzzy sets to determine a confidence that a given event is occurring

Once an event has been detected, the spacecraft operations team may choose to assign an associated action in response to the given event - change operating modes, tune a setting, prioritize a data segment, etc.

A. Derived Telemetry via Feature Extraction

Derived telemetry is calculated based on user-defined mathematical operations. Source data for the derived telemetry can come from multiple sources:

- Raw telemetry
- Previously calculated derived telemetry table, which enables analysis of long term trends, variability, waves and frequency analysis, etc.
- Ground based loads into a defined memory location (e.g. tabulated parameters, red/yellow limits)
- Messages from other spacecraft, real time ground contacts, etc.

Features are extracted into derived telemetry points, per subject matter expert (SME) definition. Essentially, the purpose of this step is to encode conversions that typically happen on the ground onto the spacecraft. To illustrate this process, we walk through an example of detecting microinjection events in the magnetosphere - a process described in detail by Nykyri et al. [27]. Microinjections are generally defined by counter-streaming electrons (particles flowing simultaneously parallel and anti-parallel to the magnetic field). The increases in electron flux coincide with troughs of magnetic fluctuations [28, 29] in a low frequency range (3-5 minutes). Table 1 shows (abbreviated for clarity) sample raw telemetry, intermediate extracted features, and derived parameters. The mnemonics are notional, but are provided as a shorthand for referencing specific elements.

1) Each sensor, C, reports a signal (counts) along an associated look direction, $\vec{L}$. The look direction can be mathematically dotted with the local magnetic field vector, $\vec{B}$, to get that sensor's local *pitch angle* (PA), relative to the magnetic field. These PAs are computed for energetic electrons in the range from 70-600 keV.
2) The flux in the pitch angle bins within 40° of the magnetic field (i.e., PAs $< 40°$ and PAs > 140 °) is summed. This parameter is denoted $f_{\parallel}$. Similarly, the flux in the pitch angle bins $40° < PA < 140°$ is summed as $f_{\perp}$. Then a final derived parameter, counterstreaming ratio, C_R is defined as $f_{\parallel}/f_{\perp}$.
3) To determine if the magnetic field is in a local trough, an extracted feature is implemented which tracks the average magnetic field over a 10 minute duration. Next, the instantaneous field magnitude is subtracted from this running average to create a *magnetic field deviation,* D_B. If the derived parameter, D_B, is negative, the field is in a trough. If it is positive, the field is at a peak.

At this point, we have extracted the pitch angle distribution from the telemetry and calculated two derived parameters: a measure of how much signal is counter-streaming along the field, C_R, and a measure of the field relative to the past few

Raw Telemetry		Extracted Features		Derived Parameters	
Magnetic Field	$\vec{B}$	Pitch Angle	PA	Magnetic Field Deviation	D_B
Sensor 1 Counts	C_1	Parallel Flux	$f_{\parallel}$	Counter Streaming Ratio	C_R
Sensor 2 Counts	C_2	Perpendicular Flux	$f_{\perp}$		
Sensor 3 Counts	C_N				
Sensor 1 Look Direction	$\vec{L_1}$				
Sensor 2 Look Direction	$\vec{L_2}$				
Sensor 3 Look Direction	$\vec{L_N}$				

Table 1 Raw telemetry (left) with extracted, intermediate features (center), leading to derived telemetry products (right).

minutes, D_B. These are the two key *physically meaningful* features that define the microinjection, per Ref. [27]. While these examples are simple calculations, MEDOS derived parameters can be complex in implementation, accounting for computational capability onboard. One of the key benefits of the derived telemetry points is to increase *trust* in the system. A scientist or SME may not intuitively know how to respond to individual signals, voltages, or telemetry traces, but if they can be converted into a physical quantity, such as "counter-streaming electrons" or "methane concentration", then the SME can apply their decades of experience in applying an event definition.

B. Event Detection

In a two-step process, a degree of membership is defined by the SME for each telemetry point and all the degrees of membership are combined to generate a probability of the event occurring.

1. Fuzzy Membership Function

A fuzzy membership function (FMF) is a function $\mu(x) : X \rightarrow [0, 1]$ which assigns a membership to each element x of a set X [30]. The set of elements along with their associated memberships is called a fuzzy set. The FMFs for MEDOS are defined for each telemetry point associated with an event using a list of telemetry values and associated memberships. The FMF is then evaluated by interpolating between the telemetry-membership pairs. Continuing with the microinjection example, Figure 1 shows the fuzzy membership function for the derived telemetry points discussed above. These fuzzy sets are easily defined from knowledge of microinjections that is readily available in the literature or from SMEs.

2. Basic Belief Assignment

Dempster-Shafer theory introduces a mathematical system for the combination of evidence and reasoning under uncertainty [31, 32]. Dempster-Shafer theory acts on a Frame of Discernment Θ, which is a set of mutually exclusive events $\Theta = \{\theta_1, \theta_2, \ldots, \theta_n\}$. The basic belief assignment (BBA) is then defined as any function $m(A) : 2^{\Theta} \rightarrow [0, 1]$

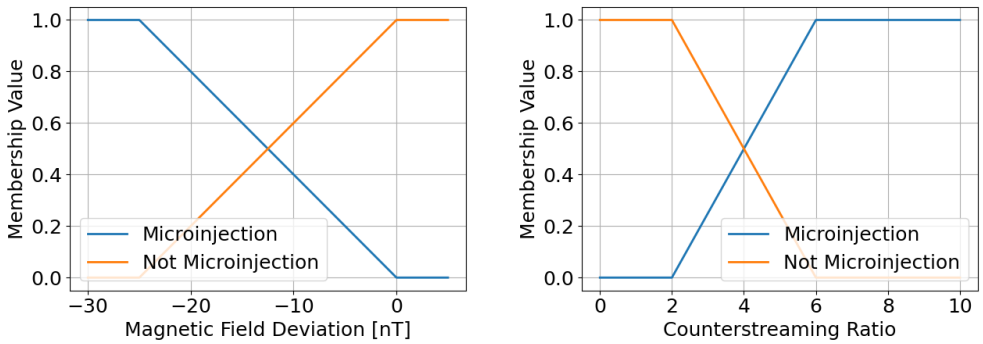

Fig. 1 Fuzzy definitions for (left) magnetic field deviation and (right) counterstreaming ratio membership for microinjection events.

where $A \subseteq \Theta$ such that

$$\sum_{A \subseteq \Theta} m(A) = 1, m(\emptyset) = 0. \tag{1}$$

$m(A)$ measures the belief committed exactly to A. If $m(A) > 0$, then A is called a focal element of Θ. If there is only one event in the A, then A is called a singleton focal element.

3. Belief Transforms

In order to obtain a BBA from a fuzzy set, a belief transform can be used. The normal BBA transform used for this project

$$m_{\text{norm}}(\{\theta_i\}) = \mu(\theta_i) / \sum_{j=1}^{n} \mu(\theta_j) \tag{2}$$

where $i = 1, 2, \ldots, n$. The normal BBA transform acts only on the singleton focal elements, which was chosen to reduce the complexity of the calculation for space flight implementation. Alternative focal elements may result in improved detection efficiency and could be further explored.

Once all BBAs are calculated, they must be combined to obtain the belief of each event. For this, we use Dempster's Rule of Combination. Given two basic belief assignments m_1 and m_2, and the associated focal elements $A_1, A_2, \ldots, A_k$ and $B_1, B_2, \ldots, B_l$ the combined BBA is defined as

$$m_{\text{demp}}(A) = \frac{\sum_{\substack{i,j \\ A_i \cap B_j = A}} m_1(A_i) m_2(B_j)}{1 - \sum_{\substack{i,j \\ A_i \cap B_j = \emptyset}} m_1(A_i) m_2(B_j)}. \tag{3}$$

4. Pignistic Probability Transform

To convert the Dempster BBA into an actionable value, a pignistic probablity transform is used. The pignistic probability is the probability that a rational person would assign to the event. There are many probability transforms to choose from [33]. The transform chosen in this work is

$$\mathrm{BetP}(\theta) = \sum_{\theta \in A \subseteq \mathbf{\Theta}} \frac{m(A)}{|A|} \tag{4}$$

Alternative pignistic probability transforms may result in improved detection efficiency and could be further explored.

5. Computational Complexity

Dempster's Combination Rule is #P-Complete, which is usually problematic for decision problems. However, in our system the frame of discernment Θ is usually small (2-3), so this is not a limiting factor in the decision computation. Additionally, for this implementation, MEDOS uses only singleton focal elements, which reduces the complexity to linear with respect to $|\Theta|$ [34].

C. Example

To demonstrate the derived telemetry, feature extraction, and and event detection, Figure 2 shows an example of how MEDOS can detect microinjections. The top panel shows the pitch angle distribution of electrons in the range of 70-600 keV. The second and third panels show the derived telemetry points of magnetic field deviation and counterstreaming ratio discussed in Section II.A. The fourth panel shows the MEDOS scores, computed using the event detection process discussed in Section II.B. As shown, MEDOS successfully detects the microinjections when counterstreaming electrons occur within troughs of the magnetic field.

III. Verification and Validation

A. Synthetic Mission Validation

To demonstrate the performance of MEDOS for spacecraft operations and validate the algorithms, a synthetic mission is conducted in which raw, level 1 (L1) spacecraft data from the Magnetospheric Multiscale Mission (MMS) are fed into MEDOS. Three operational events are considered: crossing the magnetopause, crossing the bow shock, and entrance to the outer radiation belt. These events are discussed in the following sections. A 6 month period from 2019-11-01 to 2020-04-30, composed of 52 complete orbits, is used for the synthetic mission. This date range is selected because the MMS spacecraft precess across the dayside magnetosphere during this period, as the orbits plotted in Figure 3 show, fully capturing the typical extent of the magnetopause and bow shock.

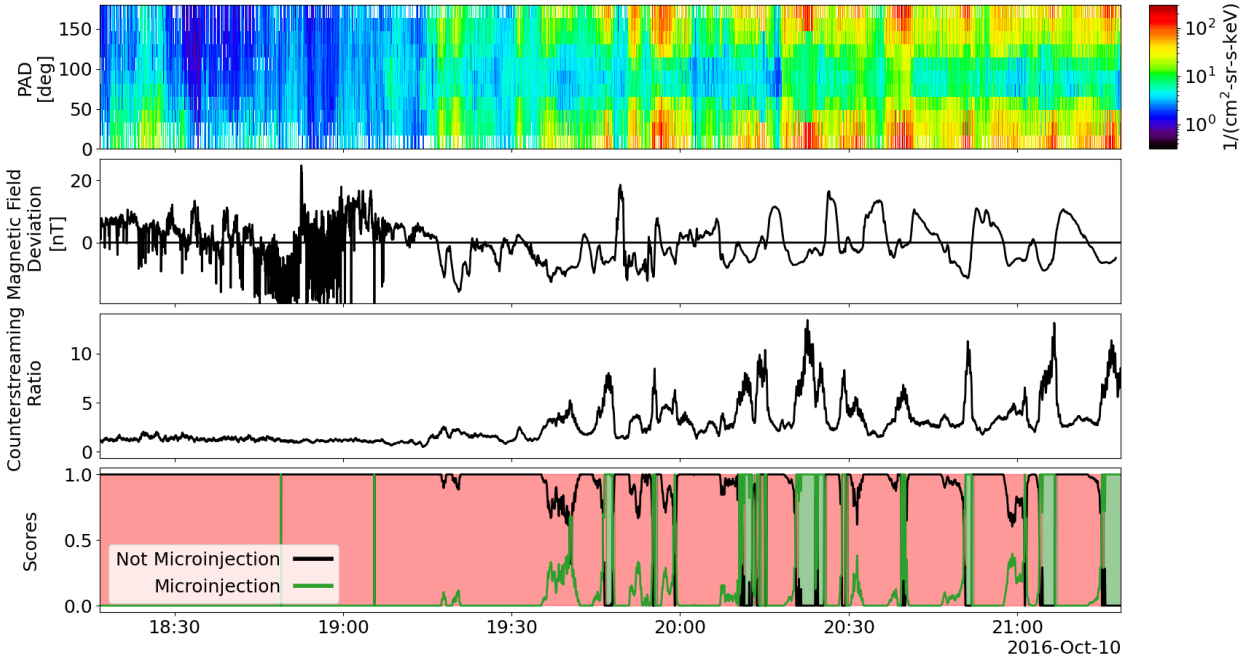

Fig. 2 Example derived telemetry and event detection of a magnetospheric microinjection event, corresponding to values from Table 1. Top - pitch angle distribution (PAD). Second, derived parameter, Magnetic Field Deviation. Third, derived parameter, Counterstreaming Ratio. Fourth (bottom), the relative scores (lines) showing the confidence that a microinjection has occurred, along with the times when MEDOS made an operational decision to flag an event as a microinjection (shaded green.)

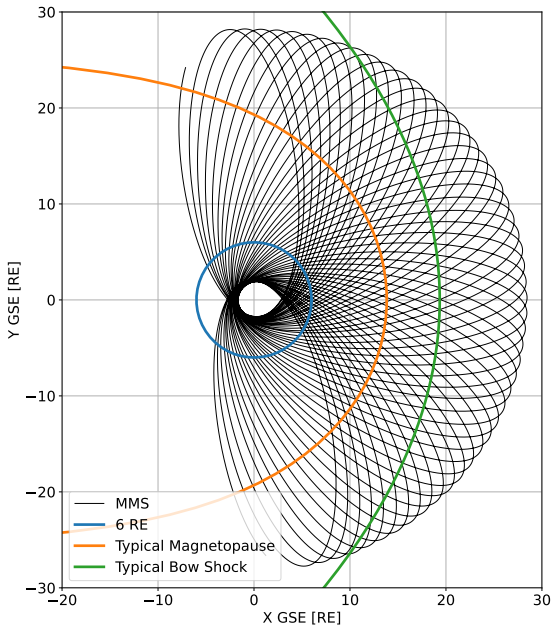

Fig. 3 MMS orbit precession from 2019-11-01 to 2020-04-30 over a typical day side pass. Notional lines for the bow shock, magnetopause and 6 Re (radiation belt entry) are noted for reference.

B. Radiation Belt Entry and Exit

The radiation belts are regions of intense, energetic particle radiation trapped in the Earth's magnetic field. These regions are torus shaped, with the inner belt ranging from 1.5-3 RE and the outer belt ranging from 4-7 RE. On many missions, spacecraft operators may instruct the spacecraft to enter a passive mode during radiation belt transit to mitigate the effects of penetrating radiation or increase the lifetime of instruments. The radiation belts are often defined in terms of L-shell (or L-value or simply L):

$$L = \frac{r}{\cos^2 \lambda}, \tag{5}$$

where r is the distance from the center of the Earth to a point on a given magnetic field line, λ is the magnetic latitude of that point, and L is the L-shell defined by the given geomagnetic field line. In other words, a given L-shell is a dipolar magnetic field line that crosses the magnetic equator at a radial distance equal to L. L-shell is a useful construct for discussing locations within a dipolar magnetic field, as is the case with the radiation belts. On MMS, the spacecraft are manually commanded from the ground to change operating modes at a fixed L-shell. However, this process is flawed for several reasons. First, the radiation belts are highly dynamic, constantly being depleted and then episodically replenished in response to space weather events [35]. Thus, the conventional understanding of a fixed radiation belt location is oversimplified so predictions of radiation belt boundaries are uncertain. Further, there are multiple approaches for calculating L-shell of which Equation 5 is only one. Different magnetic field models (dipolar, IGRF, etc.) and different coordinate systems produce different L values for the same physical location. This is illustrated in Figure 4 where the dashed line at 23:00 shows how different L models predict the spacecraft to be at either the inner edge (L-4) or the outer edge (L-8) of the outer radiation belts. Ultimately, no prediction or model will have as high degree of certainty as the actual data that is measured by the spacecraft. Therefore, it is advantageous to use the *in-situ* measurements to trigger operational actions and increase operational certainty.

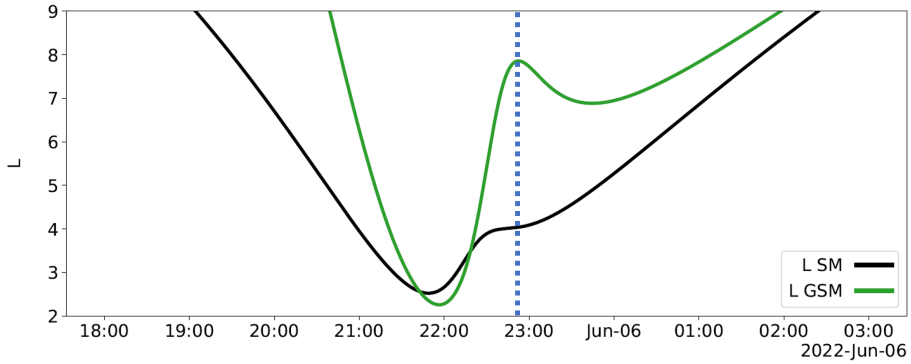

Fig. 4 At the same time (23:00, dotted line), the two models for L shell position the spacecraft either at L-8 (outer edge of the belts) or at L-4 (the inner edge of the outer belts): Geocentric Solar Magnetospheric (GSM, green) and Solar Magnetic (SM, black)

Data from the Fly's Eye Energetic Electron Spectrometer (FEEPS) instrument is used to provide MEDOS information

about the local energetic electron population [36]. Data in the highest energy bin, which contains electrons from approximately 650 keV to 1 MeV, are used to define the fuzzy memberships in either a radiation belt or not radiation belt set. Figure 5 shows the fuzzy definitions for these sets. Figure 6 shows an example of how MEDOS accurately determines the radiation belt boundaries using the FEEPS counts. To obtain statistics on MEDOS's ability to identify the radiation belt boundary, a synthetic mission is conducted using the same 6 months of data as in the region classification case. FEEPS Level 1 data is used as input.

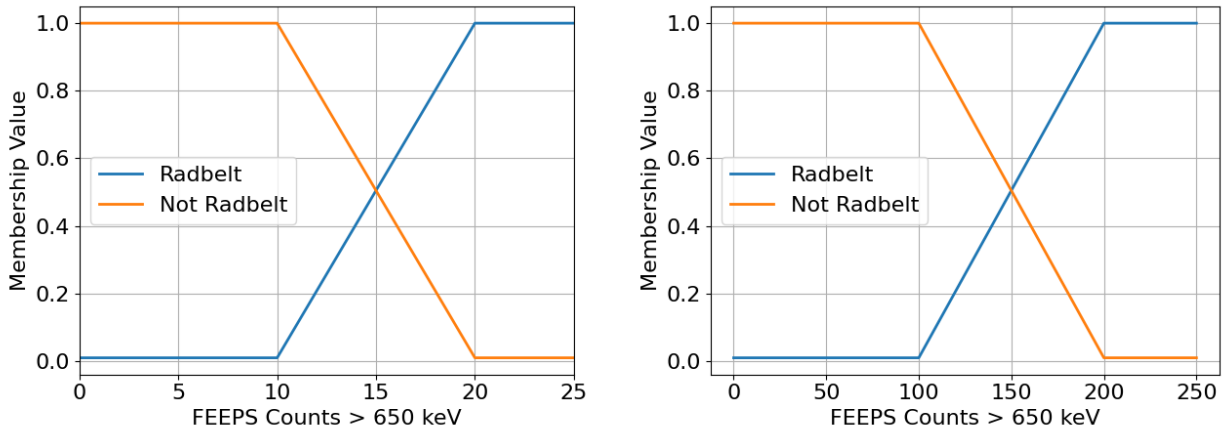

Fig. 5 Fuzzy definitions for membership in the radiation belt or not radiation belt sets for both the (left) conservative and (right) risk-tolerant settings; note the change in the x axis.

To demonstrate the adaptability of MEDOS, two different radiation belt triggers are created, a conservative trigger and a risk-tolerant trigger. When acting on the conservative trigger, MEDOS should indicate a radiation belt boundary at lower energetic electron fluxes, whereas the risk-tolerant case should not trigger until higher energetic fluxes. Figure 6 shows an example radiation belt crossing using the two different triggers. The top panel shows the measured high energy electron flux, and the second panel shows the corresponding L-shell which illustrates the entry into the radiation belt, pass through perigee, and exit of the belt. In the third panel (conservative) MEDOS triggers the radiation belt for a longer duration than the fourth panel (risk tolerant.) Note that, particularly in the risk tolerant case, MEDOS sees the the space between the inner and outer belt as safe due to the lack of high energy flux. If desired, this behavior can be easily modified to prohibit operation in the gap by either adjusting the persistence to exit, or by combining the flux with an additional parameter such as position, magnetic field strength, the lower energy flux, etc. These two cases illustrate how MEDOS can be tuned as an operational risk posture is changed - if the spacecraft needs to operate lower into the radiation belt, that is a simple update of a single parameter.

Note that in this case two event fuzzy sets are applied: *Radbelt* and *Not Radbelt*. It is not strictly necessary to implement two opposing fuzzy sets for events in this way; one could alternatively simply use a single event definition for radiation belt and trigger entry and exit based on high or low values of this single score (confidence that the spacecraft is

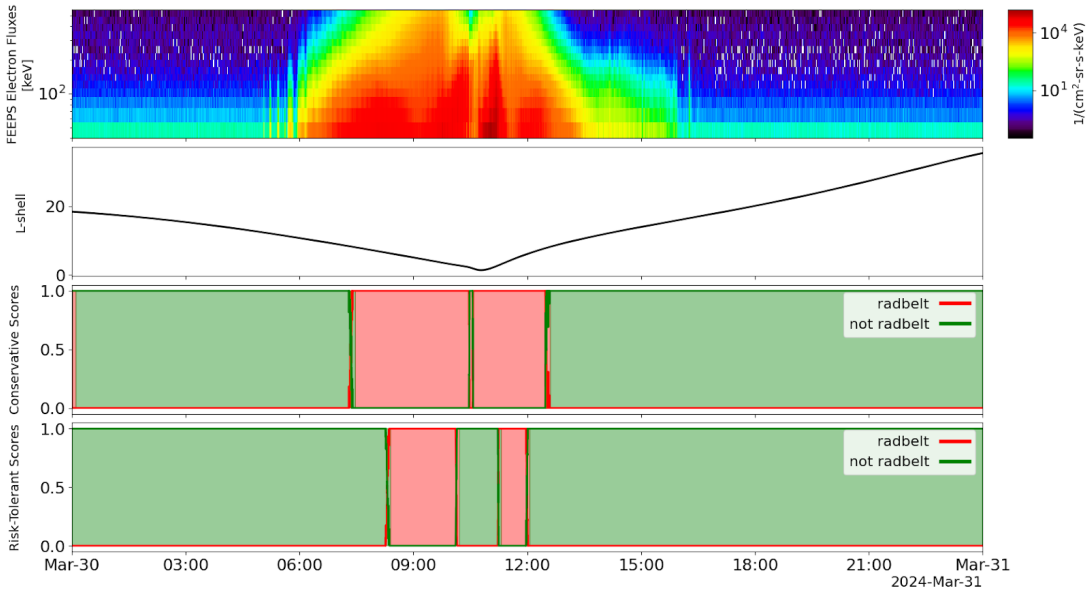

Fig. 6 Example MMS radiation belt crossing on 2020-02-11. The top panel shows the energetic electron distribution from FEEPS, the second panel shows the FEEPS counts in the highest energy bin, the third panel shows the L-shell along the MMS orbit, and the lower panel shows the MEDOS scores and decisions.

in the belt.) In this example, two definitions are used to emphasize that entering the radiation belt and exiting the belt can be considered two separate events that could be triggered from different sources based on different criteria.

Figure 7 shows the L-shells at which MEDOS triggers radiation belt entries and exits during the 6 month synthetic mission. The conservative trigger has a peak at L = 9 whereas the more risk-tolerant trigger has a peak at a lower L of 7. Note that due to the nuances of the radiation belt shape and the MMS orbit, there are some instances where MMS may leave the radiation belt and reenter causing a second trigger at a lower perceived L-Shell. In general, the most intense region of the outer radiation belt is known to range from L = 4 to L = 7. The synthetic mission results show that MEDOS is effective at detecting the increased fluxes in lower energy particles near the edge of the radiation belt, generally between L = 8 and L = 12. This would enable the spacecraft to take operational actions as needed before entering the most hazardous region of radiation. Note that the width of the MEDOS detections in the histogram of Figure 7 does not show inconsistency in the MEDOS detections, but rather emphasizes the inherent uncertainty in the L-shell approximations of the radiation belt which fail to capture the dynamic nature of space. MEDOS is making decisions based on *in-situ* measurements of energetic particles, which is precisely the hazard that concerns spacecraft operators.

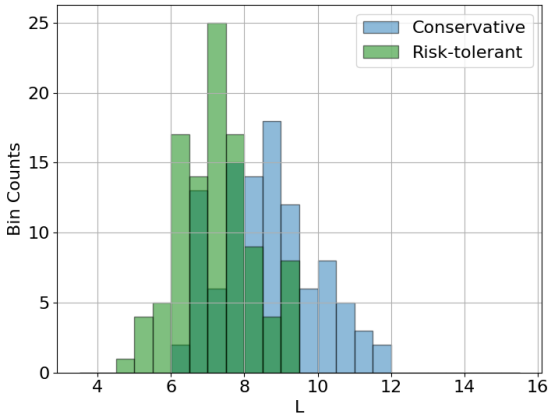

Fig. 7 Histogram of MEDOS-detected radiation belt L-shell with two different trigger values. The blue histogram represents the results with the conservative triggers. The green histogram represents the results with the more radiation-tolerant triggers.

C. Magnetopause and Bow Shock Crossings

Some of the most compelling physics in modern space physics, including the prime science targets of the MMS mission [26], occurs at the interfaces between different regions of the magnetosphere, specifically, the magnetopause and bow shock. The magnetopause divides the magnetosheath from the magnetosphere, marking the transition from where the plasma is driven by the interplanetary magnetic field (IMF) to where it is driven by the geomagnetic field. The bow shock separates the pristine solar wind from the shocked solar wind plasma in the magnetosheath.

To ensure that the rich boundary physics is captured and downloaded by the spacecraft, MEDOS should be able to identify when the spacecraft crosses one of these regions. In future missions, this capability would enable the spacecraft to automatically identify the data collected during the crossing as high value and prioritize it for high-resolution download. One interesting challenge of magnetospheric boundaries is that they are highly dynamic and move rapidly in response to variations in the solar wind, often at speeds of above 100 km/s. As a result, the boundary locations vary at timescales much smaller than a spacecraft orbit, so a spacecraft may cross the bow shock and magnetopause multiple times on a single orbit. Rather than detecting the crossings directly, it is more straightforward to have MEDOS evaluate which region it is in at each timestep. A bow shock crossing is then defined as when the region changes from solar wind to magnetosheath or vice versa. Similarly, a magnetopause crossing is defined as when the region changes from magnetosphere to magnetosheath or vice versa. Thus, the boundary crossing detection scheme is implemented in the form of a MEDOS region classifier.

We use three plasma parameters as input to the on-board region classifier: the plasma density, the electron distribution peak energy, and the electron distribution peak width. We use only the raw L1 data which is available on the spacecraft, rather than the level 2 (L2) data which have been corrected and processed on the ground. The phase space density,

$f(E, \phi, \theta)$, is computed from the raw counts as follows:

$$f(E, \phi, \theta) = \frac{\text{raw\_counts}}{F_1}, \tag{6}$$

where raw_counts is the counts matrix produced by the instrument at each timestep and F_1 is a matrix computed from ground calibration and uploaded to the spacecraft. Whereas this matrix is normally computed on the ground for each 16th of a degree of spacecraft spin, we use an averaged value to simplify the simulated on-board data processing. The plasma density is computed by taking the well-known zeroth moment of the phase space density:

$$n = 4\pi \iiint \left(\frac{2E}{m^3}\right)^{\frac{1}{2}} f(E, \phi, \theta) \sin\theta d\theta d\phi dE, \tag{7}$$

where E is the energy in eV, θ is the elevation angle, and ϕ is the azimuthal angle.

To find the peak energy, the raw_counts matrix is summed over all angular bins to produce an omnidirectional electron distribution at each timestep. The maximum value of this distribution is determined and the peak energy is the energy at which this maximum occurs. Similarly, the full width half max of the peak is determined by taking the difference of the energies closest to half the peak value on either side of the peak.

Figure 9 shows the membership values in the solar wind, magnetosheath, and magnetosphere fuzzy sets for ion density, peak energy, and peak width. These sets are defined using common knowledge of space environment parameters. Though extensive statistical studies could likely produce more rigorous definitions of the membership sets, the advantage of MEDOS's fuzzy logic approach is that robust operational autonomy can be achieved without the need for large statistical datasets. Rather, the technique is capable of "putting the scientist on the spacecraft" with membership sets that are straightforward to define.

MMS FPI (Fast Plasma Investigation [37]) Level 1 fast survey data with a time cadence of 4.5 seconds are used as input to this synthetic mission. This data product contains the raw counts collected by the instruments. MEDOS was configured with a persistence of 5, meaning that the score for one region must exceed that of another for 5 consecutive data points in order for MEDOS to decide that it is in that region. This persistence is found to provide responsive decision making (within 22.5 seconds of a given event) without being overly sensitive to short term transients. This persistence can be easily tuned to allow for an event to trigger for shorter duration events as desired.

Figure 8 shows an example of how MEDOS appropriately classifies each region and detects the boundary crossing events. The boundaries are clearly seen in the ion spectrogram which is shown in the top panel of the figure. In the given timeframe, MMS begins in the magnetosphere, crosses the magnetopause multiple times between 08:15 and 09:15, then crosses the bow shock into the solar wind at 18:48 (with two additional bow shock crossings at 19:50 and 20:30). The dynamic behavior of the boundaries are clearly seen, as MMS passes in and out of each region multiple times. In

the bottom panel, the solid lines indicate the confidence in a given region event, and the shadings indicate MEDOS's decisions for when to trigger an operational change to a new region of operation. MEDOS accurately determines the regions in this example, including the short term transitions across the bow shock noted at around 19:50 and 20:30. Note, additionally, that there are several areas (for example, around the 18:00 mark) where the region is correctly identified, but the confidence is lower - as indicated by the elevated blue solar wind confidence and significant noise on the magnetosheath confidence. This result showcases the utility of the fuzzy nature of MEDOS - even with an imperfect match to expectation, a confidence is presented and a decision can be made. This is a useful construct when deciding how confident one needs to be when triggering an action. For example, when prioritizing data as important near the bow shock, a scientist would likely trigger a "set as important" trigger with a very low confidence - a 20% chance of getting great science is still worth the potential risk of a small amount of extra downlink. Conversely, an automated thruster firing that changes the trajectory of the spacecraft may require something approaching 100% confidence in a detected precursor event.

Figure 10 shows the accuracy of these detections over the full 6 months of selected mission data. To evaluate MEDOS's performance in the synthetic mission, decisions are compared with entries in the Scientist-in-the-Loop (SitL) database. MMS employs a SitL architecture, in which low resolution data is downloaded to the ground, reviewed by a scientist who selects and ranks regions of interest for which high resolution data is then downloaded [38]. The SitL comment database is searched to identify any entries containing the terms "magnetopause," "MP," "bow shock," or "BS." The MEDOS magnetopause and bow shock crossings are grouped by orbit. For each orbit, the MEDOS decisions times are compared to the times logged in SitL entry. The results show that MEDOS accurately identifies a magnetopause crossing within 2 minutes of a SitL-selected magnetopause for 100% of orbit passes for which there is a relevant SitL entry (78 orbit passes). Similarly, MEDOS accurately identifies a bow shock crossing within 2 minutes of a SitL-selected bow shock for 96.2% of orbits for which there is a relevant SitL entry (52 orbit passes). Note that the 2 minute window is included to account for variability in the SitL selections (different personnel log the start and stop times of given events differently) and because the crossings themselves are finite time events. Indeed, the remaining few bow shock events that were not within two minutes of a SitL tagged crossing were still detected by MEDOS if the time window is expanded out to 10 minutes. This result highlights how MEDOS accurately determines the boundary locations across multiple orbits in the dynamic and uncertain space environment and is *consistent* in a way that a human operator may not be, particularly when the human operator changes frequently.

Figure 10 shows the MEDOS boundary crossings locations for both the magnetopause and bow shock. The XY location of MMS at each detected crossing is determined from the ephemeris files available at the Science Data Center. The location of each crossing in GSE coordinates is then binned and counted. For comparison, analytical models of the bow shock and magnetopause locations under both quiescent and storm conditions are overlaid on the maps [39, 40]. As shown in the figure, the MEDOS detections largely fall within expected ranges for each crossing type.

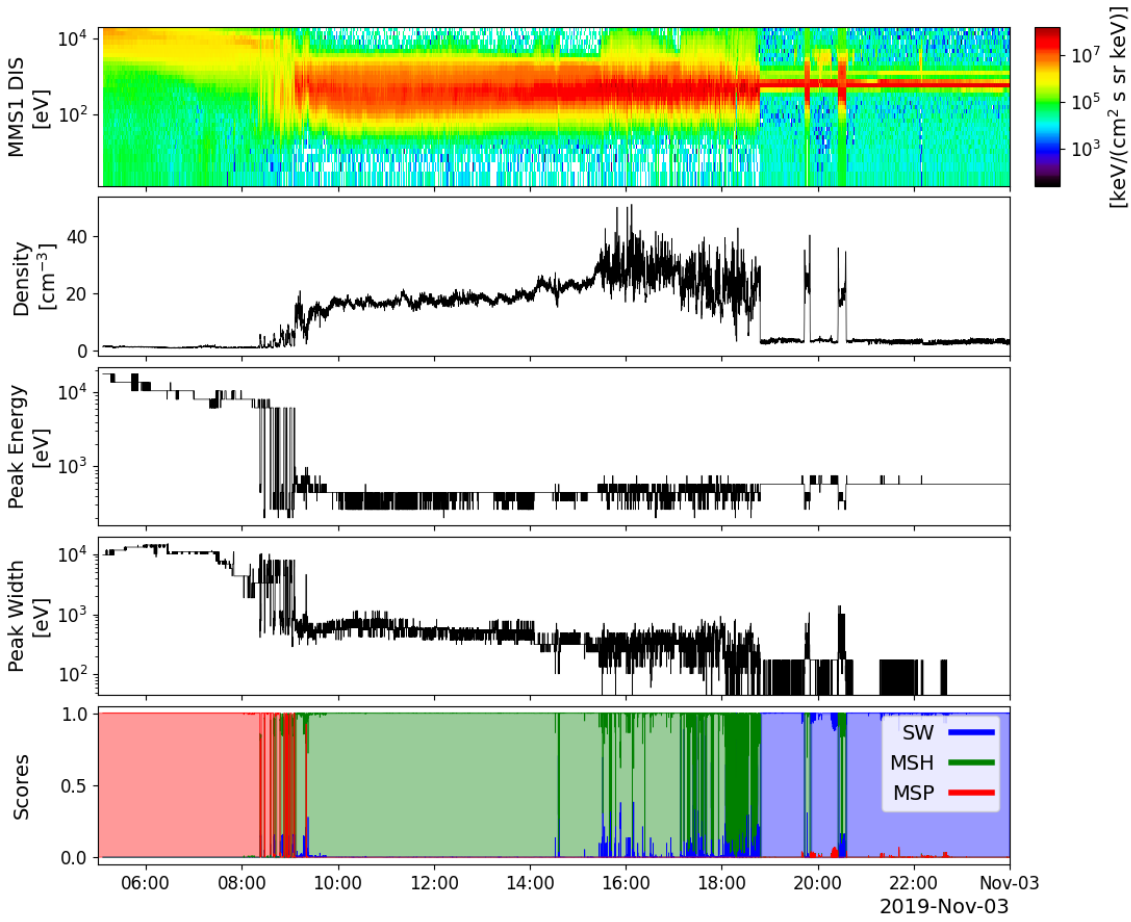

Fig. 8 Ion energy distribution (top), ion density, distribution peak energy, distribution peak width, and MEDOS scores and decisions for MMS1 on 2019-11-03 as the spacecraft crosses from the magnetosphere to the magnetosheath and into the solar wind. The lines in the bottom panel indicate the confidence of the event occurring and the shaded areas represent a MEDOS decision for an operational mode change.

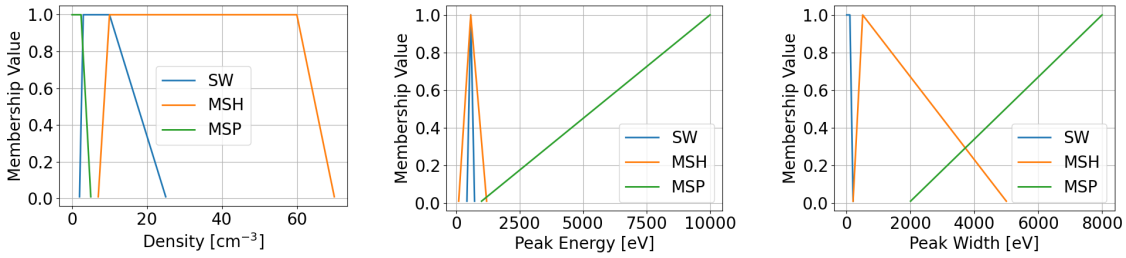

Fig. 9 Fuzzy definitions for (left) ion density, (center) plasma distribution peak energy, and (right) peak width membership in the solar wind, magnetosheath, and magnetosphere sets.

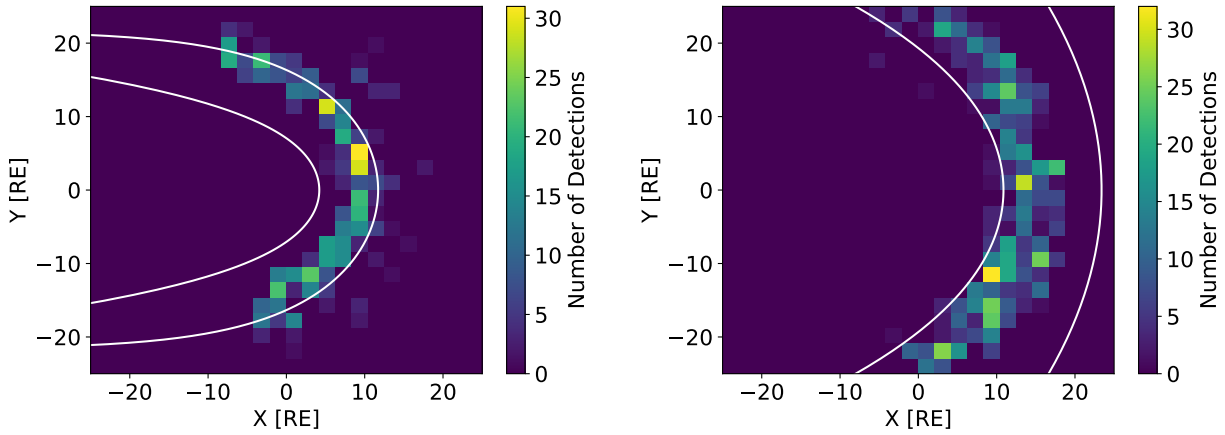

Fig. 10 2D histograms of where MEDOS detected the magnetopause (left) and bow shock (right), along with analytical models for both boundaries under quiet and stormy solar wind conditions.

D. Hardware Verification

A hardware verification was performed on the MMS flatsat testbed, which houses a flight-like CIDP (Central Instrument Data Processor) located at the University of Colorado's Laboratory for Atmospheric and Space Physics (LASP)[41, 42]. LASP houses the MMS Science Data Center and is responsible for payload operations on the MMS and for storing and serving payload data[43]. LASP developed a telemetry feeder system to transmit historic flight data to the MMS flatsat in real time to emulate in-flight operation of the MEDOS algorithms.

The compiled MEDOS code was run for several 3-day orbits to confirm that operation on the flight-like hardware (SPARC v8 LEON2-FT Processor) matched the expected simulation output from the six-month validation study. The compiled code to run on the flatsat was implemented in such a way as to be seamlessly integrated into the existing MMS flight software, leading to a planned flight demonstration on the MMS constellation in March of 2025

IV. Conclusion

Spacecraft operations can be challenging. When complex mission scenarios require operational responsiveness to an ever changing environment, it can be exceedingly difficult to plan spacecraft operations in advance. This difficulty is exacerbated when missions are far from Earth, with spotty communication, or when larger constellations require planning of multiple assets simultaneously. While AI learning algorithms are enticing for long term autonomous operation of space flight missions, these are not yet at a place where they are ready to be deployed in operational missions.

MEDOS presents a key milestone on the path towards true autonomous operation. It encodes the intelligence of subject matter experts onto the spacecraft to create derived, physically meaningful data products on board, and then uses uses those data products, much in the same way a human engineer would do, to determine if an event has occurred. A

final confidence is returned that allows the spacecraft to respond with an appropriate action based on the confidence of the stated event.

MEDOS has been validated via a synthetic re-run of a full day side pass (six months) of the MMS mission. Key events of interest to the science team, namely passing through likely reconnection zones in the bow shock and magnetopause, were detected, as well as health and safety triggers, such as entering the radiation belt. In addition, more subtle event detection of a micro-injection event was demonstrated to showcase how MEDOS can aid the scientists on the ground by identifying high value, yet hard to locate, science intervals.

In addition to validation of the algorithms, verification of the implementation has been performed on the MMS flatsat, with a planned flight demonstration on the MMS satellites scheduled for March of 2025 and potential mission infusion over the next several years. MEDOS detects events using in-situ measurements, allowing for a dynamic mission operations concept that is responsive to an ever changing space landscape. In this way, MEDOS represents a key tool for spacecraft operations and a major step forward towards trusted spacecraft autonomy.

References

[1] Freed, M., et al., "Trusted autonomy for spaceflight systems," *1st Space Exploration Conference: Continuing the Voyage of Discovery*, 2005.

[2] Abbass, H. A., Scholz, J., and Reid, D. J., *Foundations of trusted autonomy*, Springer Nature, 2018.

[3] Ambrose, R., et al., "NASA technology roadmaps: TA 4: Robotics and autonomous systems," Tech. rep., NASA, Washington DC, 2015.

[4] Starin, S. R., et al., "Fault detection and correction for the Solar Dynamics Observatory attitude control system," *AAS 2008 Guidance and Control (GN&C) Conference*, 2007.

[5] Welch, R., "Autonomous failure detection and correction on Landsat-4," *Guidance and Control Conference*, 1983.

[6] Williams, T., et al., "Operational Techniques for Dealing with Long Eclipses during the MMS Extended Mission," *2020 IEEE Aerospace Conference*, IEEE, 2020.

[7] McCabe, D., Ryan, S., Welch, D., and Fulmer, J., "AIM Autonomy Development-Long Term Care for a Deaf Spacecraft," *SpaceOps 2008 Conference*, 2008, p. 3450.

[8] Croomes, S., "Overview of the DART mishap investigation results," Tech. rep., NASA Report, 2006.

[9] Folta, D., and Hawkins, A., "Results of NASA's first autonomous formation flying experiment: earth observing-1 (EO-1)," *AIAA/AAS Astrodynamics Specialist Conference and Exhibit*, 2002.

[10] Adler, D. S., Wymer, K. B., Logue, R. M., and Hesman, B. E., "Science planning and scheduling of the James Webb Space Telescope," *Observatory Operations: Strategies, Processes, and Systems VIII*, Vol. 11449, SPIE, 2020, pp. 233–245.

[11] Su, Y., et al., "Robust anomaly detection for multivariate time series through stochastic recurrent neural network," *Proceedings of the 25th ACM SIGKDD international conference on knowledge discovery & data mining*, 2019.

[12] Hundman, K., et al., "Detecting spacecraft anomalies using LSTMs and nonparametric dynamic thresholding," *Proceedings of the 24th ACM SIGKDD international conference on knowledge discovery & data mining*, 2018.

[13] Yu, J., et al., "Telemetry Data-Based Spacecraft Anomaly Detection With Spatial–Temporal Generative Adversarial Networks," *IEEE Transactions on Instrumentation and Measurement*, Vol. 70, 2021, pp. 1–9.

[14] Harris, A., Teil, T., and Schaub, H., "Spacecraft decision-making autonomy using deep reinforcement learning," *29th AAS/AIAA space flight mechanics meeting, hawaii*, 2019.

[15] Harris, A., Valade, T., Teil, T., and Schaub, H., "Generation of spacecraft operations procedures using deep reinforcement learning," *Journal of Spacecraft and Rockets*, Vol. 59, No. 2, 2022, pp. 611–626.

[16] Elkins, J., Sood, R., and Rumpf, C., "Adaptive continuous control of spacecraft attitude using deep reinforcement learning," *2020 AAS/AIAA Astrodynamics Specialist Conference*, AIAA, 2020.

[17] Federici, L., Benedikter, B., and Zavoli, A., "Machine Learning Techniques for Autonomous Spacecraft Guidance during Proximity Operations," *AIAA Scitech 2021 Forum*, 2021.

[18] Adams, C., Kempa, B., Iatauro, M., Frank, J., and Vaughan, W., "An Overview of Distributed Spacecraft Autonomy at NASA Ames," *Proceedings of the Small Satellite Conference*, Utah State University, 2023.

[19] Labrèche, G., et al., "Artificial Intelligence for Autonomous Planning and Scheduling of Image Acquisition with the SmartCam App On-Board the OPS-SAT Spacecraft," *AIAA SCITECH 2022 Forum*, 2022.

[20] Da Silva, D. E., Barrie, A. C., Shuster, J. R., Schiff, C., Attie, R., Gershman, D. J., and Giles, B. L., "Automatic Region Identification Over the MMS Orbit by Partitioning πT Space," *arXiv preprint arXiv:2003.08822*, 2020.

[21] Innocenti, M. E., et al., "Unsupervised classification of simulated magnetospheric regions," *Annales Geophysicae*, Vol. 39, No. 5, 2021.

[22] Lu, D., and Weng, Q., "A survey of image classification methods and techniques for improving classification performance," *International journal of Remote sensing*, Vol. 28, No. 5, 2007, pp. 823–870.

[23] McComas, D., "NASA/GSFC's Flight Software Core Flight System," *Flight Software WorkshopFlight Workshop*, 2012.

[24] Quigley, M., Conley, K., Gerkey, B., Faust, J., Foote, T., Leibs, J., Wheeler, R., Ng, A. Y., et al., "ROS: an open-source Robot Operating System," *ICRA workshop on open source software*, Vol. 3, Kobe, Japan, 2009, p. 5.

[25] Bocchino, R., Canham, T., Watney, G., Reder, L., and Levison, J., "F Prime: an open-source framework for small-scale flight software systems," 2018.

[26] Burch, J., Moore, T., Torbert, R., and Giles, B.-h., "Magnetospheric multiscale overview and science objectives," *Space Science Reviews*, Vol. 199, 2016, pp. 5–21.

[27] Nykyri, K., Johnson, J., Kronberg, E., Turner, D., Wing, S., Cohen, I., Sorathia, K., Ma, X., Burkholder, B., Reeves, G., et al., "Magnetospheric multiscale observations of the source region of energetic electron microinjections along the duskside, high-latitude magnetopause boundary layer," *Geophysical Research Letters*, Vol. 48, No. 9, 2021, p. e2021GL092466.

[28] Sarafopoulos, D., "Dispersive and repetitive Pc5 mode microinjections in the inner magnetosphere," *Geophysical research letters*, Vol. 29, No. 8, 2002, pp. 26–1.

[29] Liou, Y.-L., Nykyri, K., Kavosi, S., and Ma, X., "Statistical Study of the Energetic Electron Microinjections at the High-Latitude Magnetosphere," *Journal of Geophysical Research: Space Physics*, Vol. 128, No. 10, 2023, p. e2023JA031595.

[30] Zadeh, L. A., Klir, G. J., and Yuan, B., *Fuzzy sets, fuzzy logic, and fuzzy systems: selected papers*, Vol. 6, World scientific, 1996.

[31] Shafer, G., *A Mathematical Theory of Evidence*, Princeton university press, 1976.

[32] Russell, S. J., and Norvig, P., *Artificial intelligence: a modern approach*, Pearson, 2022.

[33] Pan, W., and Yang, H., "New Methods of Transforming Belief Functions to Pignistic Probability Functions in Evidence Theory," *2009 International Workshop on Intelligent Systems and Applications*, 2009, pp. 1–5. https://doi.org/10.1109/IWISA.2009.5072973.

[34] Barnett, J. A., *Computational Methods for A Mathematical Theory of Evidence*, Springer Berlin Heidelberg, Berlin, Heidelberg, 2008, pp. 197–216. https://doi.org/10.1007/978-3-540-44792-4_8, URL https://doi.org/10.1007/978-3-540-44792-4_8.

[35] Li, X., and Temerin, M. A., "The electron radiation belt," *Space Science Reviews*, Vol. 95, No. 1-2, 2001, pp. 569–580.

[36] Blake, J., Mauk, B., Baker, D., Carranza, P., Clemmons, J., Craft, J., Crain, W., Crew, A., Dotan, Y., Fennell, J., et al., "The fly's eye energetic particle spectrometer (FEEPS) sensors for the magnetospheric multiscale (MMS) mission," *Space Science Reviews*, Vol. 199, 2016, pp. 309–329.

[37] Pollock, C., Moore, T., Jacques, A., Burch, J., Gliese, U., Saito, Y., Omoto, T., Avanov, L., Barrie, A., Coffey, V., et al., "Fast plasma investigation for magnetospheric multiscale," *Space Science Reviews*, Vol. 199, 2016, pp. 331–406.

[38] Argall, M. R., Small, C. R., Piatt, S., Breen, L., Petrik, M., Kokkonen, K., Barnum, J., Larsen, K., Wilder, F. D., Oka, M., et al., "MMS SITL ground loop: Automating the burst data selection process," *Frontiers in astronomy and space sciences*, Vol. 7, 2020, p. 54.

[39] Shue, J.-H., Chao, J., Fu, H., Russell, C., Song, P., Khurana, K., and Singer, H., "A new functional form to study the solar wind control of the magnetopause size and shape," *Journal of Geophysical Research: Space Physics*, Vol. 102, No. A5, 1997, pp. 9497–9511.

[40] Chao, J., Wu, D., Lin, C.-H., Yang, Y.-H., Wang, X., Kessel, M., Chen, S., and Lepping, R., "Models for the size and shape of the Earth's magnetopause and bow shock," *Cospar colloquia series*, Vol. 12, Elsevier, 2002, pp. 127–135.

[41] Wood, P. B., and Millwater, N., "Analysis of Mass Memory Module Performance for the MMS Mission," *2023 IEEE Aerospace Conference*, IEEE, 2023, pp. 1–7.

[42] Burch, J. L., and Torbert, R. B., *Magnetospheric multiscale: a mission to investigate the physics of magnetic reconnection*, Vol. 2, Springer, 2017.

[43] Larsen, K., Pankratz, C., Giles, B., Kokkonen, K., Putnam, B., Schafer, C., Baker, D., and Burch, J., "The MMS Science Data Center. Operations, Capabilities, and Data Availability." *EGU General Assembly Conference Abstracts*, 2016, pp. EPSC2016–10061.